Maxwell-Bloch equations for spatially inhomogeneous semiconductor lasers. II. Spatiotemporal dynamics

Ortwin Hess*
Institut für Technische Physik, Deutsche Forschungsanstalt für Luft- und Raumfahrt e.V., Pfaffenwaldring 38-40, D-70569 Stuttgart, Germany

Tilmann Kuhn†
Lehrstuhl für Theoretische Physik, Brandenburgische Technische Universität, Postfach 101344, D-03013 Cottbus, Germany
(Received 13 March 1996)

The spatiotemporal dynamics of broad-area lasers is analyzed on the basis of a space- and momentum-dependent density-matrix approach. To this means the space-dependent Maxwell-Bloch equations for the semiconductor laser (derived in our preceding paper I) are solved by direct numerical integration. The space and momentum resolved dynamics of the active semiconductor medium, described by microscopic charge-carrier distributions and nonlinear polarization functions, are treated self-consistently with the spatiotemporal dynamics of the light field. Carrier transport dynamics are approximated on the basis of an ambipolar diffusion approximation consistent with the microscopic processes. Boundary-influenced macroscopic waveguiding properties of typical conventional as well as tapered broad-area laser cavities are taken into account. The dynamics of the formation and longitudinal propagation of unstable transverse optical filamentary structures are analyzed. Simultaneous spectral and spatial hole burning with dynamical spatiospectral variations on ultrashort (ps and sub-ps) time scales are observed in the charge-carrier distributions, reflecting the interplay between stimulated emission and the relaxation dynamics of the carrier distributions as well as the polarization. The transverse hole burning leads to complex spatiotemporal patterns in the macroscopic intensity picture with different optical frequencies associated with various locations of the modelike near-field patterns. [S1050-2947(96)01509-0]

PACS number(s): 42.55.Px, 42.65.Sf, 78.20.Bh

I. INTRODUCTION

The conception of semiconductor laser structures which emit high coherent output power is one of today's technological goals in laser science. However, in the high-power semiconductor lasers, severe instabilities are frequently found responsible for the generally much inferior beam quality and spectral characteristics when compared to common semiconductor lasers with moderate output power. The fact that the transverse width of their active zone is about an order of magnitude larger than that of conventional stripe-geometry semiconductor laser diodes promotes filamentation effects. In fact, those filamentation tendencies have been known to occur in broad-area semiconductor lasers ever since they were first realized more than 20 years ago [1,2]. Considerable initiative has been invested since then to find laser designs and configurations to avoid those detrimental effects. Most technical solutions are sought in the form of monolithic arrangements and by realizing transversely structured devices, in particular, laser arrays [3,4] as well as tapered amplifiers and lasers [5]. However, even in the steady state the profile of the temporally averaged optical near field of most broad-area laser devices still appears spatially incoherent [6]. Even more vivid, the dynamical variation of the intensity distribution of the broad-area semiconductor lasers shows bewilderingly complex spatiotemporal behavior [7–9].

As much as the formation of spatiotemporal structures may be a technological drawback, the dynamic optical patterns are on *macroscopic* scales the ''fingerprints'' of the *microscopic* processes taking place inside the semiconductor laser. They thus become ''pieces of evidence'' of microscopic dynamical effects in the active semiconductor medium. The spatiotemporal patterns indeed reveal many of the otherwise concealed physical properties of the running lasers. Due to an inherent coupling of a number of different processes on microscopic and macroscopic levels, the physical properties of ''real-world'' and running devices may be profoundly different from those generally observed in the ''bare'' passive semiconductor material. A theoretical investigation consequently has to include both, macroscopic external constraints imposed by the laser structure and a spatially resolved microscopic description of the interaction between the optical field and the active semiconductor medium. Then indeed, an analysis of the mechanisms and underlying processes which lead to the self-organized, spontaneous formation of dissipative structures in the broad-area semiconductor laser devices is not only of fundamental physical and mathematical interest but also of technological relevance in the field of laser device modeling for engineering applications [10].

In spatially inhomogeneous semiconductor lasers the interaction of the optical light field and the active semiconductor medium is not only dependent on spectral properties of the semiconductor and on the local electron and hole occu-

*Electronic address: Ortwin.Hess@DLR.de
†Present address: Institut für Theoretische Physik II, Westfälische Wilhelms-Universität, Wilhelm-Klemm-Str. 10, D-48149 Münster, Germany.

pation in the conduction and valence band but also on the specific spatial location. The active medium, represented by its microscopic polarization and carrier distributions, in turn, locally acts as the source for the optical field generated by the annihilation of electron-hole pairs. In most theoretical descriptions, however, the polarization is typically adiabatically eliminated and, disregarding the wave-number dependence of the gain function, effectively the band structure of a direct-gap semiconductor is reduced to a two-level system without spectral broadening. Moreover, in many phenomenological (usually linear) approximations important nonlinear effects such as the formation of an effective dynamically changing waveguide are disregarded. This has prompted recent attempts to include the dynamics of the polarization variable on various levels. Assuming spatial homogeneity, i.e., disregarding any transport processes, Maxwell-Bloch formulations have been proposed on the basis of phenomenological two-level (instead of more realistic two-band) approximations for the active laser medium [11,12]. In a more realistic and spatially dependent Maxwell-Bloch description of semiconductor lasers, the band structure of the semiconductor medium has been included and first results on the spatiotemporal dynamics and propagation of optical filaments have been presented [9].

This paper represents the second part of our report on the theoretical description of the spatiotemporal dynamics of semiconductor lasers. In the preceding paper, which will be termed ''I'' in the following, spatially dependent semiconductor Maxwell-Bloch equations have been derived. These equations are the basis for our numerical study. We cannot but present selective results of extensive numerical simulations showing the possible complexity of the spatiotemporal dynamics of semiconductor lasers. While always considering the spatial dependence of the microscopic variables and of the optical field in the calculations, approximations in the description of the active semiconductor laser medium are made regarding the level of complexity in the explicit consideration of many-body effects in the model. In Sec. II, the formation (Sec. II A) and propagation (II B) of optical filaments in conventional broad-area semiconductor lasers is studied. In Sec. II C, we will demonstrate that in the broad-area laser, spectral and transverse spatial hole burning occur simultaneously and discuss their dynamics occurring in the ps- and sub-ps time scale. The possibility of longitudinal spatiotemporal structure formation resulting in ultrashort pulsations is addressed in Sec. III. Finally, representing the combination of a long laser cavity with a transversely large stripe, we will discuss the spatiotemporal dynamics of flared broad-area lasers in Sec. IV. Section V concludes the article.

II. SPATIOTEMPORAL DYNAMICS OF BROAD-AREA LASERS

Based on the microscopic spatially resolved semiconductor model derived and discussed in I, we will use the general Maxwell-Bloch formulation for spatially inhomogeneous semiconductor lasers for the description of the spatiotemporal dynamics of edge-emitting broad-area semiconductor lasers. In the numerical simulations, relevant microscopic effects of the active semiconductor medium are considered self-consistently with the macroscopic properties of the laser devices. In a first step we have disregarded the Coulomb enhancement in the numerical simulations which is generally expressed by the internal field. In our analysis we will particularly concentrate on the interrelations between microscopic and macroscopic processes in the active laser medium which we consider in the numerical simulations simultaneously and together with the macroscopic device properties. To this means the coupled system of partial differential equations [Eqs. (67)–(74) of I] is solved by direct numerical integration. Technically the equations consist of two blocks of equations: the ''macroscopic'' subsystem of equations (consisting of two wave equations for couterpropagating complex optical fields [Eq. (67) of I] and an ambipolar diffusion equation [Eqs. (73) with (74) of I]) and the ''microscopic'' system [Eqs. (69)–(72) of I]. In the case of the edge-emitting semiconductor lasers considered here, numerical modeling requires consideration of the fast and slow dynamics in two dimensions [transverse (x) and longitudinal (z)] in space and, with the assumption of a spherical Fermi surface, in one dimension in momentum (k). The fast dynamics of the ''microscopic'' subsystem [Eqs. (69)–(72) of I] is governed by the intraband scattering times $\tau_{e,h}(k)\approx 50$ fs and the dipole dephasing rate $\tau_p=(\tau_e+\tau_h)/2\approx 50$ fs. The decay of the distribution functions $f^{e,h}$ due to nonradiative recombination, however, occurs on a ns time scale ($\gamma_{nr}\approx 5$ ns). The system (69)–(72) of I is thus a system of *stiff* differential equations. For its integration we employ a method of finite differences, using a second-order *implicit* scheme, where the interval of wave-numbers k which typically ranges from 0 to 20 (in units of the inverse of the exciton Bohr-radius a_0) is discretized in $N_k = 100$ discrete steps. In the ''macroscopic'' subsystem of *hyperbolic* and *parabolic* partial differential equations (67) and (73) of I, the round trip time $\tau_r=2n_lL/c$ of the optical field in the semiconductor laser cavity of length $L=250$ μm is about 3 ps. It is the relevant time scale for the dynamics of the optical fields $E^{\pm}$. The nonradiative relaxation time of the carrier density τ_{nr} being in the order of 5 ns, is larger by three orders of magnitude. For the numerical integration of the system of partial differential equations (67) and (73) of I, the *hopscotch* method is used as a general scheme. The operators are discretized by the *Lax-Wendroff* method. In space, the number of transverse and longitudinal discretization points N_x and N_z, respectively, varies. Typically $N_z=11$, $N_x=201$ were used. To resolve the propagation of the optical fields inside the laser, i.e., the intracavity dynamics, we used an increased longitudinal resolution, e.g., $N_z=201$, $N_x=201$. At every time step all microscopic and macroscopic quantities are self-consistently determined. The material and structural parameters are summarized in Table I.

A. Dynamic transverse filamentation

Due to the width w of the transverse stripe contact being typically one order of magnitude larger than in the case of a single-stripe laser, broad-area laser devices can emit considerably high output power and are frequently used to pump solid-state lasers or as powerful light sources in optical communication systems. Often, in order to facilitate production steps, they are manufactured as a pure gain-guided device and the lower cladding lacks any imposed transverse

TABLE I. Fundamental material and device parameters as used in the simulations, pertaining to typical high-power GaAs/AlGaAs-semiconductor lasers.

L (cavity length)	:	$200 \ldots 1500\ \mu m$
d (thickness of active layer)	:	0.15 μm
n_c [Ref. index of the cladding layers (GaAlAs)]	:	3.35
n_l [Ref. index of active layer (GaAs)]	:	3.59
λ (laser wavelength)	:	815 nm
R_1 (front facet mirror reflectivity)	:	0.33
R_2 (back facet mirror reflectivity)	:	0.33 (0.99)
τ_{nr} (nonrad. recombination time)	:	5 ns
a_0 (exciton Bohr radius)	:	1.243×10^{-6} cm
m_0 (mass of the electron)	:	$9.109\,387\,9 \times 10^{-31}$ kg
m_e (effective electron mass)	:	$0.067\ m_0$
m_h (effective hole mass)	:	$0.246\ m_0$
E_g (semiconductor energy gap)	:	1.4262 eV
D_p (diffraction coefficient)	:	18×10^{-6} m
η_i (injection efficiency)	:	0.5
Γ (confinement factor)	:	0.55/0.54
α_w (absorption)	:	30 cm^{-1}
v_{sr} (surface recombination velocity)	:	10^6 m/s

waveguiding structure. As neither optical confinement nor the confinement of the injected charge carriers diffusing in the transverse x direction are provided by the device structure, the possibility of self-focusing (filamentation) and multitransverse mode operation exists in the broad-area lasers. Figure 1 shows the spatially resolved dynamics of the near-field output intensity $I(x,z=0,t)=T_1|E^-|^2/Z$ of a broad-area laser with $Z=n_l/(\varepsilon_0 c)$ being the optical wave resistance in the semiconductor medium and $T_1=1-R_1$ being the transmissivity of the front mirror. In Fig. 1 the laser has a transverse width $w=50\ \mu$m and is strongly pumped by applying an electrical injection current $J=1$ A (switched on at $t=0$), corresponding to about five times its threshold current value ($J_{th}\approx 200$ mA). Here and also in the subsequent illustrations, brightly white colored areas correspond to high values of the signal intensity (carrier density), dark shading indicating low output power (carrier density). The transverse coordinate is indicated by x and given in μm. The first striking impression of Fig. 1 is the complexity in variation of different regimes of spatiotemporal patterns. Due to the strong electrical excitation, even the first intensity maximum of the relaxation oscillation shows three maxima. Moreover, in between relaxation oscillation peaks, the near field of the laser still displays meandering filaments of moderate intensity. We note that this behavior more closely coincides with the recently experimentally observed near-field single-strike streak-camera measurements [13] than initial simulations using constant carrier-distribution and phase-relaxation times [9] in contrast to the microscopically determined momentum- and density-dependent rate distribution used here. The succession of dynamically more complex with less structured periods is an indication for space time induced intermittency. The development of dynamic filamentary structures shows that with sufficient pumping multitransverse mode oscillations can be excited ''from the start.''

Figures 2 and 3 show the start-up dynamical behavior of a 100 μm wide broad-area laser for two different pumping conditions (Fig. 2: $J=2J_{th}$, Fig. 3: $J=3J_{th}$). The gray-scale

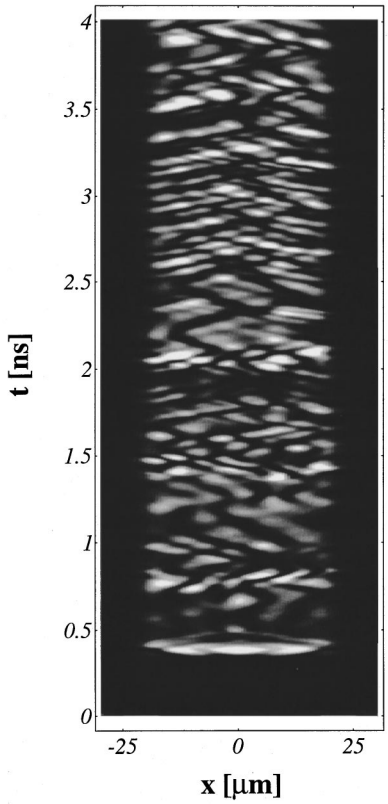

FIG. 1. Start up dynamics of a 50 μm wide broad area laser. Light shading corresponds to high values of the near-field intensity $I(x,z=0,t)$, dark shading indicates low intensity values. The width of the absorbing layers which are located on both sides of the laser stripe is 10 μm. The injection current is turned on at $t=0$ and held constant in time. The time-window extends over a period of about 4 ns and shows the formation and transverse migration of optical filaments after the first relaxation-oscillation pulse.

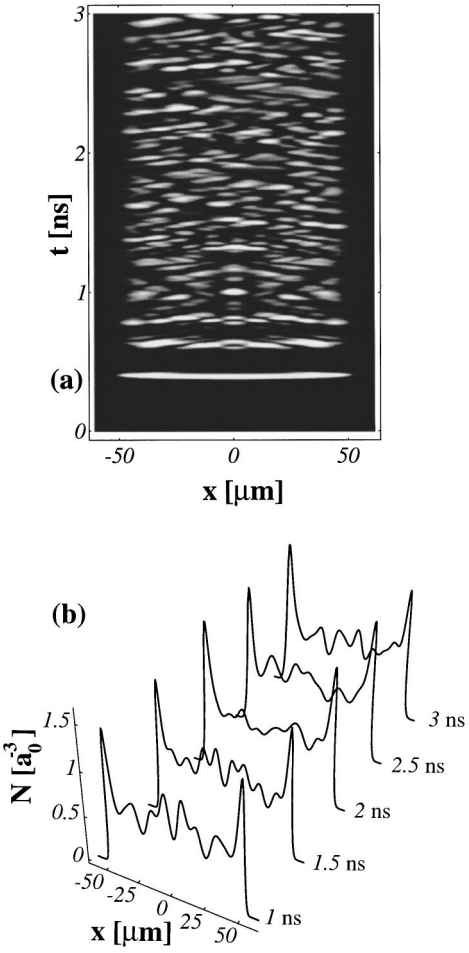

FIG. 2. Spatiotemporal dynamics of a 100 μm wide moderately pumped ($J=2J_{th}$) broad-area laser. The injection current is turned on at $t=0$. (a) Gray-scale plot of the output intensity. Light shading corresponds to high values of the signal intensity, dark shading indicates low output power. (b) Transverse cuts of the corresponding spatiotemporal variation of the charge-carrier density.

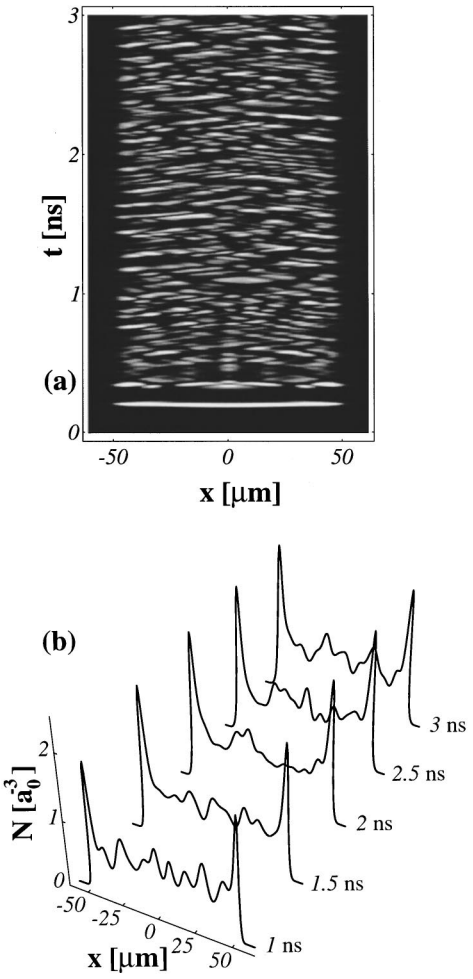

FIG. 3. Spatiotemporal intensity trace pertaining to the same laser structure as in Fig. 2, but strongly pumped at $J\sim 3J_{thr}$.

plots in Figs. 2(a) and 3(a) display the spatiotemporal evolvement of the output intensity; Figs. 2(b) and 3(b) show sequences of transverse cuts of the spatiotemporal variation of the electron-hole density. With the moderate pumping current values applied in Fig. 2, the first relaxation-oscillation peak is still transversely homogeneous. However, soon thereafter, a larger number of optical filaments are ''born'' than in the case of the laser with $w=50$ μm (Fig. 1). The influence of an elevated rate of electrical pumping is directly documented in the increase of the current density values at the transverse edges of the laser stripe and the larger number of modelike transverse intensity structures leading to rising spatiotemporal complexity (c.f. Fig. 3 in comparison to Fig. 2).

In both broad-area laser structures, the optical filaments are highly unstable due to a transverse modulational instability [14] which leads to a very complex intensity pattern as time preceeds. Effectively, the filaments seem to migrate across the laser output facet. The processes which lead to this peculiar behavior are a consequence of the relaxation times of the carrier density being larger than that of the optical field, leading to a localization of filaments of high intensity in wave-guiding channels formed by the carrier density. Dynamically, the carrier density is locally depleted by a filament of high intensity. The optical filament is thus located in a region of low gain (low carrier density) and relatively high refractive index. At the same time it is surrounded on both sides by regions of higher gain and lower refractive index. By the process of gain guiding the filament thus provides itself with the dielectric waveguide which is necessary for its support during propagation in the laser cavity. With uniform injection of charge carriers, however, the local carrier density outside the filament is not being depleted by stimulated emission, and consequently, rises quickly to levels above the threshold charge-carrier density. A new optical filament is thus created. The induced waveguides persist considerably longer than the actual presence of the filaments which had initially been their origin, thus becoming a means of memory for this filament to follow. It nonlinearly interacts with the previous filament, thereby destabilizing it. The result is a vividly irregular and fundamentally chaotic interaction of optical filaments. The gain-guiding processes inside the laser cavity also ensure that by sustaining relatively stable high values of the density at the edge of the laser stripe the optical field has created its own optical waveguide, i.e. an effective waveguide is formed which leads to transverse gain narrowing (filamentation). Following this global focusing effect transverse modulations appear on a finer scale which pro-

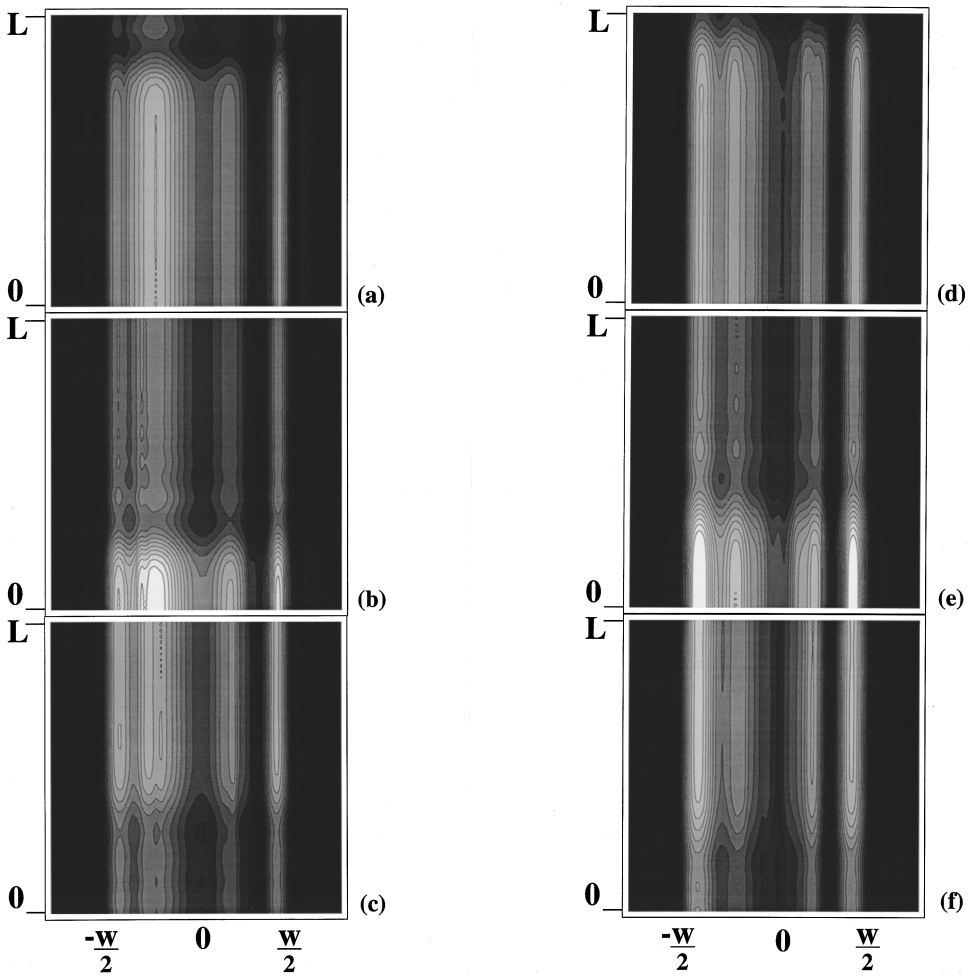

FIG. 4. Propagation of the filamentary structures in the broad-area laser. The individual plots display snapshots showing the equi-intensity regions of the intracavity intensity $I(x,z,t_{(i)}) \sim (|E^+(x,z,t_{(i)})|^2 + |E^-(x,z,t_{(i)})|^2)$, with $i=a,\ldots,f$ at the times (a) $t_{(a)}=t_0$, (b) $t_{(b)}=t_0+1$ ps, (c) $t_{(c)}=t_0+2$ ps, (d) $t_{(d)}=t_0+2.8$ ps, (e) $t_{(e)}=t_0+3.5$ ps, and (f) $t_{(f)}=t_0+4.5$ ps. Dark shading corresponds to low intensity and bright colors to areas of high intensity. The out-coupling facet (mirror reflectivity $R_1=0.33$) is located at the lower edge of each square. The highly reflecting back-coupling mirror ($R_2=0.99$) is at the upper edge. The longitudinal extension corresponds to 250 μm; the total transverse width ($w=50$ μm) is 70 μm.

mote finer scale filamentation instabilities through a transverse modulational instability.

The whole filamentation process in the broad-area semiconductor laser thus is a result of continuous competition between the antiguiding effects, i.e., the carrier-induced refractive index δn being negative, and subsequent self-focusing on the one hand, and on the other hand diffraction and the tendency of the filaments to follow the gain (which is proportional to the density of charge carriers). Although a steady state is never reached, we observe a typical width of these filaments $w_f \approx 10-15$ μm [15]. This value is determined by the combined influence of diffraction (diffraction coefficient $D_p = 1/2K_z = \lambda/4\pi n_l$), i.e., by the light wavelength λ, and by diffusion [16]. Thus for a 100 μm wide broad-area stripe roughly six to ten filaments are amplified and supported.

B. Longitudinal propagation of intensity-fronts causing transverse filament migration

In the preceding section, we have identified the characteristic dynamics of transverse filaments in typical broad-area lasers to be the result of a combination of nonlinear effects: self-focusing, filamentation, and transverse modulational instabilities. In the analysis we have been focusing on the spatiotemporal evolution of the light signal which is emitted at one of the facets of the laser—the configuration corresponding to an experiment. Our theoretical model, however, also allows to monitor the dynamics *inside* the laser. This viewpoint which is generally concealed to experiments visualizes the propagation of the optical filaments within the laser, their interactions with each other or with the boundaries of the laser cavity as well as their amplification and absorption. As an example we select a time period of 4.5 ps following the post-relaxation-oscillation regime of a broad-area laser with transverse width $w=50$ μm, electrically pumped at about twice its threshold. Figures 4(a) to 4(f) show six snapshots of the spatial distribution (in the $x-z$ plane) of the sum of the intensity $I(x,z,t_{(i)}) \sim |E^+(x,z,t_{(i)})|^2 + |E^-(x,z,t_{(i)})|^2$ taken at times $t_{(i)}$ about $t_0=8.7$ ns after the laser is switched on. Each $x-z$ plane is discretized on a 101×101 grid. The brighter the shading between the contour lines, the higher the intensity. In the longitudinal z direction the coordinates have been

scaled such that the actual spatial extent of the laser corresponds to the entire area shown in each frame in the six plots. In our model configuration the out-coupling facet which is located at the lower edge of each square has the natural reflectivity $R_1=0.33$. At the upper edge of each frame a high reflectivity ($R_2=0.99$) back-coupling mirror is placed. The laser has a length of 250 μm and its total width of 70 μm is occupied by a contact stripe of width $w=50$ μm. Strongly absorbing layers, which each have a width of 10 μm are located symmetrically on each side of the current stripe. In Fig. 4(a) it is one dominant optical filament extending from the top down to the bottom of the frame which can be located somewhat left from the center with respect to the transverse position. In Fig. 4(b) this filament has propagated towards the bottom of the frame, gaining in intensity during this process. At the same time a fine, thinner filament at the very right edge of the laser stripe is amplified (the frames still contain the absorbing cladding layers) which also propagates towards the out-coupling mirror. Due to the (natural) reflectivity $R_1=0.33$ of the lower facet of the cavity, two-thirds of the intensity of the filamentary structure leave the laser, while one-third is internally reflected back into the resonator. It is these two-thirds of the intensity of the filaments which is observed from the outside when monitoring the dynamics of the intensity along the transverse coordinate. Of this structure only the change in time of the lower edge at the out-coupling mirror is seen, where the areas of high and low intensity pertain as long as the filamentary structure propagates through the cavity. At the time $t_{(c)}=t_0+2$ ps, i.e. in Fig. 4(c), the intracavity intensity is thus lower than in the two frames before. However, a new filamentary structure can already be identified in Fig. 4(c), which in the following is amplified during its propagation towards the highly reflecting facet of the cavity at $z=L$. The propagation now is in opposite direction to the one of the filamentary structure in Fig. 4(a) and 4(b). Due to its high reflectivity, however, only a small percentage (1%) of the intensity of these filaments is transmitted at this facet with reflectivity $R=0.99$. There, most of the filamentary structure is reflected, gains in intensity and has effectively changed its direction of propagation [Figs. 4(d) and 4(e)]. In Figs. 4(d) and 4(e), similar situations as in Figs. 4(c) and 4(d), respectively, are reached. However, direct comparison of Fig. 4(e) and Fig. 4(b) shows that after reflection at the upper cavity end the transverse filamentary structure is profoundly different than before. In particular, when only monitoring the transverse dependence of the intensity, the major part intensity seems to have radically jumped from one filament to another one. The observation of all frames, however, then reveals that the apparently diagonally migrating optical filaments (*transverse mode hopping*) are the result of one filament of the filamentary structure receiving more gain than another one during the propagation in the cavity.

C. Spatiotemporal carrier dynamics: Simultaneous spectral and spatial hole burning

In the numerical simulations, the determination of the space-time dependence of the optical field on the basis of the macroscopic system of equations [(67) and (73) of I] requires at every spatial point the perpetual evaluation of the microscopic carrier distributions and polarization functions. By the help of the relaxation-time approximation, the influence of carrier-carrier and carrier-phonon scattering processes on the relaxation of the polarizations $p_{nl}^{\pm}(k,\mathbf{x},t)$ as well as the electron and hole distributions $f^{e,h}(k,\mathbf{x},t)$ is accounted for using characteristic relaxation rates $\tau_p^{-1}(k)$ and $\tau_{e,h}^{-1}(k)$, respectively. In Fig. 5, snapshots of the dependence of the variation $\delta f^e(k,\mathbf{x},t)=f^e(k,x,z=0,t)-f^e_{eq}(k,x,z=0,t)$ on the wavenumber k and the transverse position x at the output facet of the broad-area laser are shown. The spectral as well as the spatial position of the ''holes'' constantly varies. Moreover, the spectral location of the deepest hole varies across the laser structure. Thus the laser not only shows a broad spectrum of wavelengths, but also the main frequency of the laser, say, on its left edge, differs from the one on its right side. This results in perpetual highly irregular frequency variations and shifts.

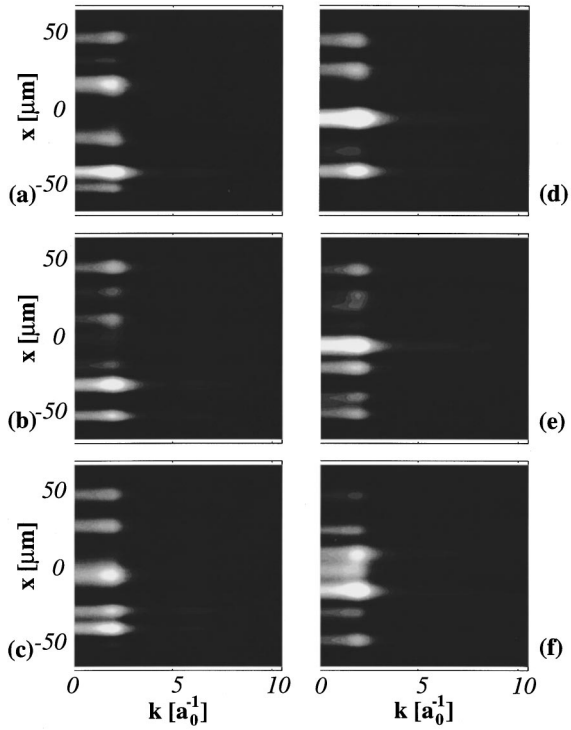

FIG. 5. Snapshots of the transverse dependence of the distribution $\delta f^e(k,\mathbf{x},t)=f^e(k,\mathbf{x},t)-f^e_{eq}(k,\mathbf{x},t)$ at the output facet ($z=0$) of a broad-area laser with transverse width $w=100$ μm and $J\approx 2J_{th}$. The snapshots are taken after the relaxation oscillations with the time between successive time frames being 100 ps.

III. LONGITUDINAL SPATIO-TEMPORAL DYNAMICS: SELF-MODELOCKING AND ULTRASHORT PULSE FORMATION

Having seen that the unstable filaments propagate inside the broad-area lasers in the form of a transversely structured high-intensity front it is only natural to ask what might happen if the longitudinal cavity-length L of a stripe-geometry laser is considerably increased from $L=250$ μm to $L=1000\ldots2000$ μm. In order to separate the transverse filament dynamics from possible longitudinal spatiotemporal phenomena, we have considered a semiconductor laser structure with a cavity length $L=1500$ μm which is sufficiently

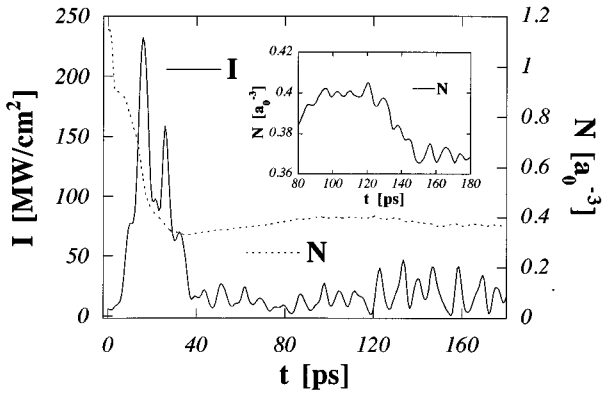

FIG. 6. Dynamics of the transversely averaged intensity $I(t)=\langle I(x,z=0,t)\rangle_x$ and charge-carrier density $N(t)=\langle\Sigma_{\mathbf{k}} f^{e(h)}(\mathbf{k},x,z=0,t)\rangle_x$, where $f^{e(h)}$ is the electron (hole) distribution function, $\mathbf{k}$ the carrier momentum, and $\langle\cdot\rangle_x$ the transverse average, in a time sequence of about 180 ps. The insert shows a blowup of the density.

narrow ($w=5\,\mu$m) to support only one transverse mode. As expected, the smaller transverse stripe width prevents the filamentations. Surprisingly, however, instead of approaching quasi-steady-state (*cw*) operating conditions typically known for narrow lasers, the long laser shows continuous pulsations. Figure 6 shows a typical sequence of short optical pulses in the 5 to 20 ps regime. The pulses of the transversely averaged intensity at the front laser facet, i.e. $\langle I(x,z=0,t)\rangle_x$, is paired with corresponding depressions (note the differences in scales) in the carrier density. In addition to the short pulsations, the ps pulses are typically superimposed onto longer pulse structures with durations of about 0.2 to 0.5 ns. The numerical results reveal that this spontaneous formation of short optical pulses is a consequence of a breaking up of the intracavity high-intensity front. A representative sequence of snapshots showing the spatial distribution of the intracavity intensity $I(x,z,t)$ (Fig. 7) illustrates the formation and propagation of an optical pulse structure in the laser. Detailed analysis of our numerical simulations indicate that the origin for the formation of these short pulses lies in the combination of dynamic transverse self-focusing with spatiotemporal variation of gain and absorption along the laser cavity. With the laser cavity effectively being longer than an internal coherence length, the active semiconductor medium consists for short time periods and in restricted spatial regions with characteristic electron and hole states of absorbing areas located next to amplifying states. Once a pulselike intensity structure is created, it is these (saturably) absorbing regions in the active zone which initiate the laser to self-mode lock. The consequence is the formation of a train of pulse structures as observed in Fig. 6. However, due to the pronounced spatial and temporal variation of both dispersive and absorptive states in the laser, the resulting sequence of pulses constitutes a suite of short but irregularly appearing intensity spikes.

IV. FLARED BROAD-AREA LASERS

In the flared semiconductor laser, the transverse width of the current stripe increases from one end of the laser cavity

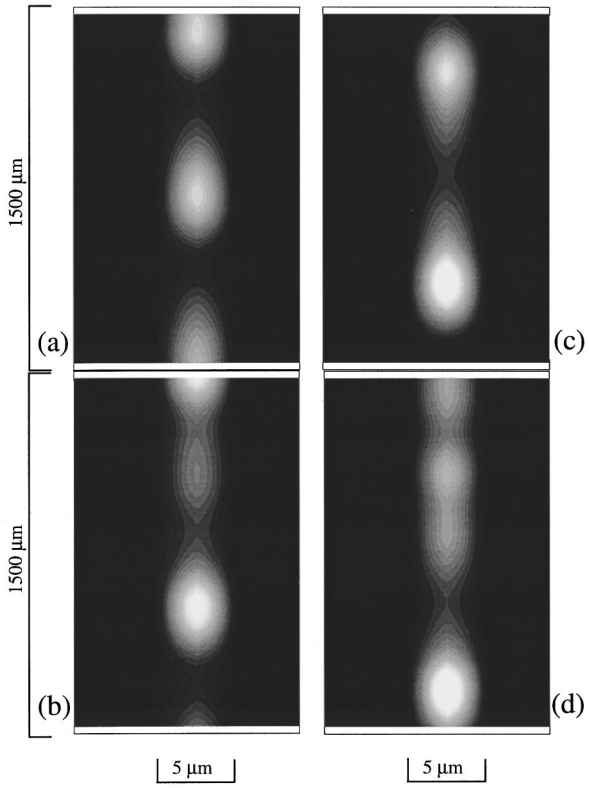

FIG. 7. Snapshots of the spatial distribution of the intracavity intensity $I(x,z,t_{(i)})\sim|E^+(x,z,t_{(i)})|^2+|E^-(x,z,t_{(i)})|^2$ of a long ($L=1500\ \mu$m) but narrow ($w=5\,\mu$m) high-power semiconductor laser. The snapshots are extracted from the simulation at (a) $t_{(a)}=t_0$, (b) $t_{(b)}=t_0+2.2$ ps, (c) $t_{(c)}=t_0+4.4$ ps, and (d) $t_{(d)}=t_0+6.6$ ps, with $t_0=2115$ ps after starting carrier injection. Bright shading indicates high intensity, dark shading stands for low intensity values. The characteristic sequence shows the formation and propagation of a self-mode-locked optical pulse.

to the other one. With the flared broad-area lasers typically having a length of 1 to 2 mm, a narrow stripe width w_1 of about 5 to 10 μm at one side and at the signal-out-coupling facet with a transverse width w_2 ranging from 100 to 200 μm, they thus effectively represent the combination of the two laser structures considered previously. By direct integration of a low-power coherent laser structure with a high-power (usually incoherent) broad-area part it is hoped to increase the output power of the laser and still suppress most of the salient spatial and spatiotemporal filamentation effects. Note that frequently, these tapered structures are technically realized for operation as amplifiers (rather than lasers) into which a coherent optical beam is injected from the narrow side. For the case of an amplifier where the reflectivity of the out-coupling facet has been reduced below 10^{-4} by application of antireflection coatings an analysis of the static properties of filament formation has recently been given [17].

Figure 8 displays snapshots of the intracavity intensity $I(x,z,t_{(i)})\sim|E^+(x,z,t_{(i)})|^2+|E^-(x,z,t_{(i)})|^2$, with $i=a,b,c,d$ at about 1.7 ns after the start-up of the laser extracted from the simulation about every 15 ps. The narrow end of the flared amplifying stripe contact has width $w_1=10\ \mu$m, a wide out-coupling facet with width $w_2=100\ \mu$m. The facets of the laser cavity have the values $R_1=R_2=0.33$.

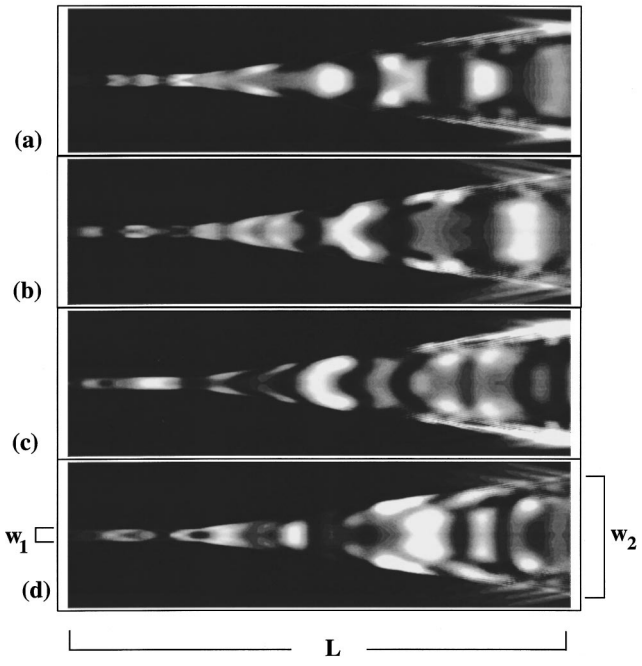

FIG. 8. Propagation of optical filaments in a flared broad-area semiconductor laser. The individual plots display snapshots of the intracavity intensity $I(x,z,t_{(i)}) \sim (|E^+(x,z,t_{(i)})|^2 + |E^-(x,z,t_{(i)})|^2)$, with $i=a,b,c,d$ taken at intervals of 15 ps about 1.7 ns after the start-up of the laser. Dark shading corresponds to low intensity and bright colors to areas of high intensity. The out-coupling facet is located at the right side of the laser. Its transverse stripe width is $w_2=100$ μm. The stripe width at the left side of the laser is $w_1=100$ μm. The longitudinal extension corresponds to 1000 μm. Both facets are uncoated, i.e., $R_1=R_2=0.33$.

Indeed, the formation of multiple optical filaments is prevented at the narrow end of the laser. However, filamentation obviously cannot be avoided at the wide end of the cavity ($w_2=100$ μm). In addition to the filamentation there, internal reflection of the filaments at this cavity end and back propagation towards the left side causes complex spatiotemporal intensity distributions and thus dynamically incoherent optical fields. Among the various complex spatiotemporal intensity structures frequently a horseshoelike shape can be observed. This mode structure which is characteristic for an unstable resonator reflects the tendency of the laser to effectively avoid the plane-plane Fabry-Perot resonator by forming its own dynamic waveguiding structure.

V. CONCLUSIONS

The spatiotemporal dynamics of spatially inhomogeneous semiconductor lasers has been studied theoretically on the basis of Maxwell-Bloch equations which include both, space dependence and the momentum dependence of the charge carriers and the polarization. The coupled system of equations (67)–(74) of I describes the dynamics of the counterpropagating optical fields together with the microscopic properties of the spatially inhomogeneous active laser medium. The waveguiding properties of the double heterostructure are taken into account. Within this model, the mechanisms and consequences of spectral as well as spatial hole burning are considered in the relaxation-time approximation. The momentum- and density-dependent relaxation rates for the carrier distributions as well as for the polarization include carrier-carrier scattering and carrier-phonon interactions. Thus the processes leading to the decay of the electronic dipole moment, which affects the decay of the phase coherence of the polarization in the active semiconductor medium, are included.

Results of numerical simulations based on the system of coupled nonlinear partial differential equations (67)–(74) of I were presented. In the broad-area laser, self-focusing effects lead to multitransverse mode behavior and filamentation leading to strikingly complex spatiotemporal patterns. The spatiotemporal patterns in the near-field output intensity and the density of charge carriers result from self-focusing and filamentation effects as well as transverse modulational instabilities. Depending on excitation conditions or the shape of the laser resonator, interactions among and coupling between the dynamically changing optical filaments may cause regular, periodic or high-dimensional chaotic behavior. The numerical simulation of the spatiotemporal dynamics of the broad-area laser by direct integration of the partial differential equations reveals that the combination of self-focusing effects with diffusion of charge carriers and spatial and spectral nonlinearities in the distribution of the gain leads to multitransverse mode behavior. The defects, patterns, and symmetry breaking phase transitions are identified as the *macroscopic* ''fingerprints'' of the *microscopic* processes taking place inside the lasers which manifest themselves, e.g., in the simultaneous relevance of spectral and spatial hole-burning effects in the microscopic charge carrier distributions of the broad-area laser. The results of the numerical simulations are in striking agreement with corresponding experimental single-streak-camera measurements which for the first time show and thus confirm the complex spatiotemporal dynamics seen in the computed near-field of broad-area semiconductor lasers [13].

In the flared broad-area lasers, the optical field initially is spatially uniform in the narrow end of the device. At its wide edge, however, filamentation sets in—similar as in the laser with a conventional resonator geometry. Due to reflections at the outcoupling facet, the filaments are back coupled into the resonator and thus strongly influence its behavior. In spite of some improvements in spatial coherence as compared to the conventional broad-area laser, the consequences of such a monolithic integration of ''low-power'' coherent and ''high-power'' incoherent laser sections into one device still lead to dynamically rapidly changing optical filaments at the outcoupling facet and, in particular, to strong phase fluctuations. It is those fast spatiotemporal variations of the optical phase which is hard to control but vital for the realization of coherent high-power semiconductor laser sources.

Clearly, the fundamental microscopic physical effects determine the behavior of the whole device. On the other hand, we have shown that the macroscopic boundary conditions imposed by the device architecture strongly influence the processes occurring on microscopic scales and thus should not be considered without taking the former into account.

Knowledge about the mechanisms and underlying processes which lead to the self-organized, spontaneous formation of dissipative structures in the high-power semiconductor laser devices may thus be at the same time of fundamental significance and relevant for the design of new devices in which such effects may be controlled or avoided.

ACKNOWLEDGMENTS

We particularly would like to thank H. Opower, G. Mahler, and E. Schöll for many interesting and fruitful discussions. One of us (T. K.) wishes to thank the Deutsche Forschungsgemeinschaft for financial support within the framework of the Sonderforschungsbereich 296.

[1] J. C. Dyment, Appl. Phys. Lett. **10**, 84 (1967).
[2] G. H. B. Thompson, *Physics of Semiconductor Laser Devices* (Wiley, New York, 1980).
[3] N. W. Carlson, *Monlythic Diode-Laser Arrays* (Springer-Verlag, Berlin, 1994).
[4] D. Botez, in *Diode Laser Arrays*, edited by D. Botez and D. R. Scrifres (Cambridge University Press, Cambridge, 1994), pp. 1–71.
[5] D. R. Welch and D. G. Mehuys, in *Diode Laser Arrays*, edited by D. Botez and D. R. Scrifres (Cambridge University Press, Cambridge, 1994), pp. 72–122.
[6] R. J. Lang *et al.*, IEEE J. Quantum Electron. **QE-30**, 685 (1994).
[7] O. Hess, *Spatio-Temporal Dynamics of Semiconductor Lasers* (Wissenschaft und Technik Verlag, Berlin, 1993).
[8] O. Hess, Chaos Solitons Fractals **4**, 1597 (1994).
[9] O. Hess, S. W. Koch, and J. V. Moloney, IEEE J. Quantum Electron. **QE-31**, 35 (1995).
[10] G. R. Hadley, in *Diode Laser Arrays*, edited by D. Botez and D. R. Scrifres (Cambridge University Press, Cambridge, 1994), pp. 180–225.
[11] C. M. Bowden and G. P. Agrawal, Phys. Rev. A **51**, 4132 (1995).
[12] J. Yao, G. P. Agrawal, P. Gallion, and C. M. Bowden, Opt. Commun. **119**, 246 (1995).
[13] I. Fischer, O. Hess, W. Elsäßer, and E. Göbel (unpublished).
[14] H. Adachihara *et al.*, J. Opt. Soc. Am. B **10**, 658 (1993).
[15] This value has recently been confirmed in single-strike streak-camera measurements [13].
[16] D. Merbach, O. Hess, H. Herzel, and E. Schöll, Phys. Rev. E **52**, 1571 (1995).
[17] L. Goldberg, M. R. Surette, and D. Mehuys, Appl. Phys. Lett. **62**, 2304 (1993).